Camera Augmented Mobile C-Arm (CAMC): Calibration, Accuracy Study, and Clinical Applications

Nassir Navab*, Sandro-Michael Heining, and Joerg Traub

Abstract—**Mobile C-arm is an essential tool in everyday trauma and orthopedics surgery. Minimally invasive solutions, based on X-ray imaging and coregistered external navigation created a lot of interest within the surgical community and started to replace the traditional open surgery for many procedures. These solutions usually increase the accuracy and reduce the trauma. In general, they introduce new hardware into the OR and add the line of sight constraints imposed by optical tracking systems. They thus impose radical changes to the surgical setup and overall procedure. We augment a commonly used mobile C-arm with a standard video camera and a double mirror system allowing real-time fusion of optical and X-ray images. The video camera is mounted such that its optical center virtually coincides with the C-arm's X-ray source. After a one-time calibration routine, the acquired X-ray and optical images are coregistered. This paper describes the design of such a system, quantifies its technical accuracy, and provides a qualitative proof of its efficiency through cadaver studies conducted by trauma surgeons. In particular, it studies the relevance of this system for surgical navigation within pedicle screw placement, vertebroplasty, and intramedullary nail locking procedures. The image overlay provides an intuitive interface for surgical guidance with an accuracy of <1 mm, ideally with the use of only one single X-ray image. The new system is smoothly integrated into the clinical application with no additional hardware especially for down-the-beam instrument guidance based on the anteroposterior oblique view, where the instrument axis is aligned with the X-ray source. Throughout all experiments, the camera augmented mobile C-arm system proved to be an intuitive and robust guidance solution for selected clinical routines.**

Index Terms—**Augmented reality visualization, C-arm navigation, image-guided surgery.**

I. Introduction

The mobile C-arm is an essential tool in everyday trauma and orthopedics surgery. With increasing numbers of minimally invasive procedures, the importance of computed tomography (CT) and fluoroscopic guidance is continuously growing [1]–[4]. Considerable effort has been undertaken to optimize the use of CT and C-arm imaging especially in combination with external tracking systems to enable intraoperative navigation [5]–[9]. These systems crucially change the current procedure and add additional technical complexity. Most of these systems require the fixation of a dynamic reference base (DRB) and involve invasive registration procedures using acquired surface points of the bone in the tracking space. Despite the benefit of more accurate and robust access routes (e.g., [10]–[12] for pedicle approach in spinal interventions), their drawback is the additional invasive registration and referencing procedures [13] and the complexity introduced by additional hardware components like an optical infrared tracking system reducing the operating room working space due to the line-of-sight requirement.

One technique for 2-D navigation is the *virtual fluoroscopy* proposed by Foley *et al.* [14]. They overcome the limitation that only a single planar fluoroscopic view is available at a given time by combining the C-arm with an external tracking system. They coregister the C-arm and the optical navigation coordinate system, in which the instruments are tracked. This enables the real-time projection of the tracked instruments onto the fluoroscopic images. With biplanar acquisition of X-ray images, ideally in orthogonal position, an advanced 3-D navigation interface can then be provided.

Nowadays, the combined use of mobile C-arms, that are capable of 3-D reconstruction, and a tracking system that provides navigation information during surgery offers advanced three dimensional navigation based on intraoperative reconstructed data [15]. Such solutions, often referred to as *registration-free navigation*, are commercially available for various trauma and orthopedics surgery applications [16], [17]. Here, a C-arm system with 3-D reconstruction capability is calibrated and tracked within the same coordinate system as the surgical instruments are tracked in. Thus, the cone beam reconstruction of the C-arm is within the tracking space and is by default coregistered with the tracked instruments. This technique has a considerable advantage over navigation based on preoperative CT data, especially for the deformable organs and when the patient is positioned differently than during CT acquisition. Hayashibe *et al.* [18] combined the registration free navigation approach with *in situ* visualization. They use an intraoperative tracked C-arm with reconstruction capabilities and a monitor that is mounted on a swivel arm providing volume rendered views from any arbitrary position.

However, in the surgical workflow, intraoperative 3-D imaging is only possible at distinct points during the intervention, e.g., to visualize the quality of fracture-reduction or to

Manuscript received December 19, 2008; revised March 27, 2009; accepted April 01, 2009. First published May 26, 2009; current version published June 30, 2010. This work was supported by Siemens Medical Solutions SP. *Asterisk indicates corresponding author.*

*N. Navab is with the Chair for Computer Aided Medical Procedures, Technische Universität München, 80333 München, Germany (e-mail: navab@cs.tum.edu).

S. M. Heining is with the Chirurgische Klinik und Poliklinik, Klinikum der LMU, 81377 München, Germany (e-mail: sandro-michael.heining@med.uni-muenchen.de).

J. Traub is with the Chair for Computer Aided Medical Procedures, Technische Universität München, 80333 München, Germany (e-mail: traub@cs.tum.edu).

Color versions of one or more of the figures in this paper are available online at http://ieeexplore.ieee.org.

Digital Object Identifier 10.1109/TMI.2009.2021947

plan and control the position of implants. During 3-D image acquisition no manipulation like drilling or implant positioning is possible, i.e., the different steps of the surgical procedure are still carried out under 2-D fluoroscopic imaging. Thus, radiation exposure to both patient and surgical staff, is often inevitable. In some surgical procedures even the direct exposure of the surgeon's hand cannot be avoided [19]. The applied radiation dose decreased using computer assisted surgery solutions [20].

In the last decade, the first medical augmented reality (AR) systems, which enhance the direct view of the surgical target with virtual data, were introduced. Exemplary setups and applications for *in situ* visualization include augmented reality operating microscopes for neurosurgery [21], [22], head mounted operating binoculars for maxillofacial surgery [23], augmentation of magnetic resonance imaging (MRI) data onto an external camera view for neurosurgery [24], and systems based on head mounted displays [25]–[28]. A system based on a tracked semi-transparent display for *in situ* augmentation has also been proposed [29]. Sielhorst *et al.* present an extensive literature review of medical AR in [30].

Most of the proposed *in situ* visualization systems augment the view of the surgeon or an external camera with coregistered preoperative data. A few medical AR systems, including CAMC, directly use the intraoperative images for augmentation. Stetten *et al.* [31] augment the real time image of an ultrasound transducer onto the target anatomy. Their system is called *sonic flashlight* and it is based on a half silvered mirror and a flat panel miniature monitor mounted in a specific arrangement with respect to the ultrasound plane. Fichtinger *et al.* [32] proposed a similar arrangement of a half transparent mirror and a monitor rigidly attached to a CT scanner. This system allows for *in situ* visualization of one 2-D fluoro CT slice *in situ*. A similar technique was proposed for the *in situ* visualization of a single MRI slice [33], however with additional engineering challenges to make it suitable for the MR suite. Leven *et al.* [34] augment the image of a laparoscopic ultrasound into the image of a laparoscope controlled by the daVinci telemanipulator. Feuerstein *et al.* [35] augment the freehand laparoscopic view with intraoperative 3-D cone-beam reconstruction data following a registration-free strategy, i.e., tracking C-arm and laparoscope with the same external optical tracking system. Wendler *et al.* [36] augment the real time image of an ultrasound probe with synchronized functional data obtained by a molecular probe that measures gamma radiation. These systems are based either on 3-D medical imaging modalities or in case of ultrasound and fluoro CT of 2-D slices. In contrast to these, X-ray follows a 2-D *projective* geometry. Thus its augmentation will be only possible by an image taken by a camera positioned exactly at the center of X-ray projection geometry, i.e., X-ray source position. In [37] and [38], we proposed to attach an optical video camera to the housing of the gantry of a mobile C-arm. Using a double mirror system and thanks to a calibration procedure performed during the construction of the system, the X-ray and optical images are aligned for all simultaneous acquisitions. If the patient does not move, the X-ray image remains aligned with the video image. This makes the concept quite interesting for medical applications, particularly those who are currently based on continuous X-ray or fluoroscopic imaging. The concept was originally proposed for its use in guiding a needle placement procedure [37] and for X-ray geometric calibration [39], [40].

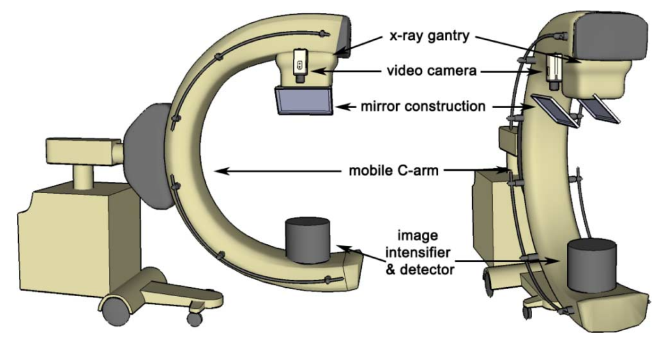

Fig. 1. Camera-augmented mobile C-arm system setup. The mobile C-arm is extended by an optical camera.

Here we demonstrate the feasibility of the re-engineered video augmented mobile C-arm system for distal interlocking of intramedullary implants, vertebroplasty procedures, and pedicle screw placement through a cadaver study.

This paper also describes the setup for the camera augmented mobile C-arm system as well as its associated calibration method. We then present several applications in orthopedics and trauma surgery. The accuracy of the image overlay and radiation dose are also evaluated. An *ex vivo* experiment was conducted to measure the implant placement accuracy and applied radiation dose within a simulated surgical scenario. The phantom and cadaver experiments demonstrated the clinical relevance and simplicity of the use of camera augmented mobile C-arm system.

II. System Overview

The camera augmented mobile C-arm system extends a common intraoperative mobile C-arm by a color video camera (cf. Section II-A and Fig. 1). A video camera and a double mirror system are constructed such that the X-ray source and the camera optical center virtually coincide (cf. Section II-B3b). To enable an image overlay of the video and X-ray image in real time (cf. Figs. 7 and 8) a homography has to be estimated that maps the X-ray image onto the video image (cf. Section II-B3c) taking the relative position of the X-ray detector implicitly into account (cf. Section II-B2). The mobile C-arm is used in a configuration with the X-ray source above the patient and the bed to ensure the visibility of the patient by the video camera. This is in an upside-down configuration compared to the standard clinical use of mobile C-arms with the X-ray source under the operation table. In such standard use, the X-ray images are left–right flipped so that the images fit the viewpoint of the physician. In order to augmented the camera view, in our case the X-ray images are not flipped. This again fits the viewpoint of the surgeon as the C-arm is upside-down. A nonflipped X-ray image could be misleading for a physician, who is not use to it. However, this flipping effect is easy to get used to by the surgeons thanks to its augmentation on the anatomy. Most of our clinical partners never noticed this flipping in regard to the standard use simply because the superimposition of X-ray on optical images leaves no room for confusion.

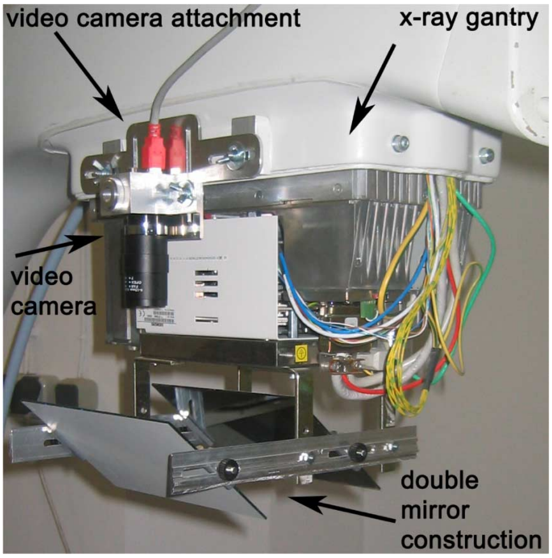

Fig. 2. Video camera and the double mirror construction is physically attached such, that it has the same optical center and optical axis as the X-ray source.

A. System Components

The C-arm used in the initial setup and in the experiments is a Siremobile Iso-C 3-D from Siemens Medical Solutions (Erlangen, Germany), a system that is used in our clinical laboratory for both phantom and cadaver studies. The video camera is the Flea from Point Grey Research, Inc. (Vancouver, BC, Canada). The camera includes a Sony $1/3''$ progressive scan CCD, Color with 1024×768 pixel resolution at a frame rate of 30 FPS. The camera is connected via Firewire connection (IEEE-1394) to the visualization computer, which is a standard PC extended by a Falcon framegrabber card from IDS Imaging Development System GmbH (Obersulm, Germany). The construction to mount the camera and the mirrors are custom made within our workshop. Without a mirror construction, it is physically impossible to mount the video camera such that the X-ray source and the camera optical center virtually coincide. The mirror within the X-ray direction has to be X-ray transparent in order not to perturb the X-ray image quality. For the experiments presented in this paper, the camera was attached on the side of the gantry. Another valid and practical option is to attach the camera on the side of the X-ray source in front of its housing. Note that the choice between these two options has no effect on the calibration process or accuracy of the superimposition. We also developed and adopted an interactive touchpad based user interface for visualization and guidance (cf. Section II-C).

B. System Calibration

The calibration procedure has to be performed only once during the initial attachment of the video camera and the double mirror construction to the gantry of the C-arm. It is valid as long as the optical camera and the mirror construction are not moved with respect to the X-ray gantry. The most recent system setup incorporates the rigidly mounted construction into the housing of the C-arm gantry. Furthermore, a combined optical and X-ray marker is introduced to ensure the overlay quality.

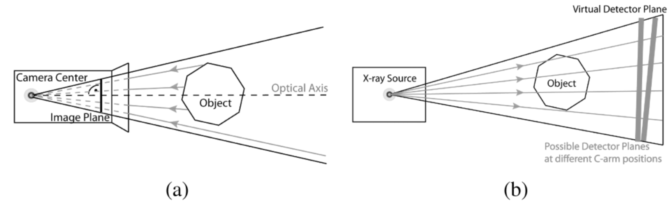

Fig. 3. Basic principles and geometric models of optical camera and X-ray imaging: (a) optical camera and (b) X-ray imaging.

This quality assurance has to be performed before every operation. During the pilot studies in the operation room, we have to assess the quality and validity of the one-time calibration throughout the lifecycle of the system. The geometric models of optical and X-ray imaging will be shortly introduced followed by the calibration routine composed of distortion correction, physical attachment of the video camera, and estimation of the homography.

1) Model of Optical Cameras: Optical cameras, especially CCD cameras, are in general modeled as a pinhole camera. The camera model describes the mapping between 3-D object points and their corresponding 2-D image points using a central projection. The model in general is represented by an image plane and a camera center [cf. Fig. 3(a)]. The lens and the CCD sensor are in general in the same housing. This creates a fixed relationship between image plane and optical center. The projection geometry is commonly represented by $x = PX$ with $P \in \mathbb{R}^{3\times 4}$ the projection matrix, $X \in \mathbb{P}^3$ the object point in 3-D and $x \in \mathbb{P}^2$ its corresponding point in the image in projective space [41], [42].

2) Model of X-Ray Imaging: The X-ray imaging is generally modeled as a point source with rays going through the object and imaged by the detector plane [cf. Fig. 3(b)]. X-ray geometry is often modeled using the same formulation as the optical video camera and with the same set of tools of projective geometry. However, in contrast to the optical camera model, the X-ray source and the detector plane are not rigidly constructed within one housing. Therefore, the X-ray source and the detector plane have geometric nonidealities caused by bending of the C-arm. Compensation for changes in the relative position and orientation between X-ray source and detector plane can be accomplished using a method based on the definition of a virtual detector plane [43]. This method consists of imaging markers located on the X-ray housing near the X-ray source and imaged on the borders of detector plane. The warping of these points to fixed virtual positions, often defined by a reference image, guarantees fixed *intrinsic* parameters, i.e., source-to-detector, image center, pixel size and aspect ratio. The new 3-D C-arms have more stable rotational movements and allow us to compute the required warping to the virtual detector during an offline calibration procedure.

3) Three Step Calibration Procedure: The system calibration procedure is described and executed in three consecutive steps.

a) Step 1: Distortion Correction: Both the optical video camera and the X-ray imaging have distortions. The optical camera distortion is estimated and corrected using standard computer vision methods. We use a nonlinear radial distortion model and precompute a lookup table for fast distortion

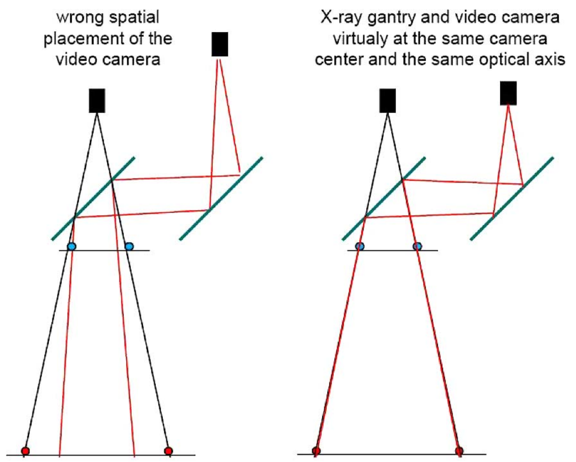

Fig. 4. Video camera has to be attached such that its optical camera center virtually coincides with the X-ray image source.

correction [44]. The radial lens distortion of the video camera is modeled by $X_{\mathrm{un}} = D + X_{\mathrm{dist}}$ with $X_{\mathrm{un}} \in \mathbb{R}$ the undistorted point on the image, $X_{\mathrm{dist}} \in \mathbb{R}$ the distorted one, and $D = X_{\mathrm{dist}}(k_1 r^2 + k_2 r^4 + \cdots + k_i r^{2i})$ a polynomial function of the distortion coefficients k_i. The distortion coefficients are computed using well-known calibration techniques using a calibration pattern with known 3-D geometry [45], [46]. The X-ray geometric distortion depends on the orientation of the mobile C-arm with regard to the earth's magnetic field, thus is dependent on angular, orbital and wig–wag (room orientation) angles. For precise distortion correction, the C-arm has to be calibrated for every orientation. Look up tables provided by the vendor correct for the geometrical X-ray distortion for most common poses of the C-arm. For C-arms with solid-state detectors instead of X-ray image intensifiers, distortion is a minor problem and is often taken into account by system providers.

b) Step 2: Alignment of X-Ray Source and Camera Optical Center: The next step after the distortion correction consists of the positioning of the camera such that its optical center coincides with the X-ray source. This is achieved if a minimum of two undistorted rays, both optical and X-ray, pass through two pairs of markers located on two different planes (cf. Fig. 4). For one of the modalities, e.g., X-ray, this is simply done by positioning two markers on one plane and then positioning two others on the second plane such that their images coincide. This guarantees that the rays going through the corresponding markers on the two planes intersect at the projection center, e.g., X-ray source. Due to parallax, the second modality will not view the pairs of markers as aligned unless its projection center, e.g., camera center, is also at the intersection of the two rays defined by the two pairs of markers.

In practice, this alignment is achieved by mounting the camera using a double mirror construction (cf. Fig. 2) with the support of a visual transparent bi-planar calibration phantom (cf. Fig. 6). Our calibration phantom consists of five X-ray and optically visible markers on two transparent planes. The phantom is placed on the image intensifier of the C-arm. The markers on the far plane are rigidly attached spherical CT markers with 4 mm diameter (CT-SPOTS, Beekley Corporation, Bristol, CT). The markers on the near plane are aluminum

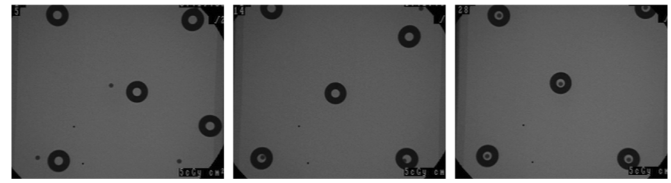

(a) (b) (c)

Fig. 5. Sequence of X-ray images during the alignment of the markers on the bi-planar calibration phantom: (a) unaligned, (b) intermediate, and (c) aligned.

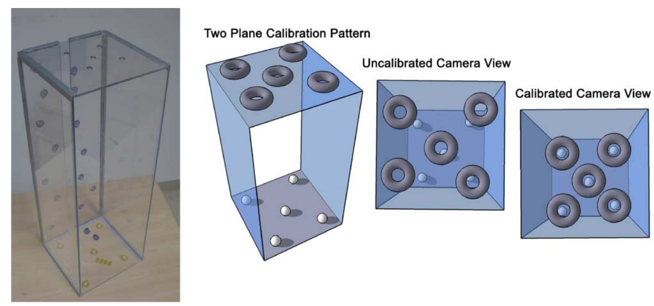

Fig. 6. Bi-planar calibration phantom consists of X-ray and vision opaque markers. On the far plane at the bottom of the calibration phantom five spherical markers are rigidly attached. On the near plane there are five rings attached such that they can be moved and aligned with the spherical markers within the X-ray image.

rings that are moved such that they are pairwise overlaid with their spherical counterparts on the far plane in the X-ray image. In order to align all markers a series of X-ray images are acquired while moving the ring markers on the upper plane (cf. Fig. 5). Once all markers are aligned in the X-ray image, the optical video camera is attached such that all markers are also overlaid in the video image. The calibration phantom and the C-arm must not move until the final placement of the video camera is confirmed, i.e., the centers of all spherical markers are projected exactly in the center of the ring markers in the video image. Since this calibration step is a one time procedure during manufacturing of the device, a manual procedure for the research prototype is an acceptable solution. For a final assembly of the CAMC unit an algorithm enabling automatic extraction and visual servoing of the marker points and an apparatus for the placement in its optimal position could be realized with some additional engineering efforts.

c) Step 3: Homography Estimation for Image Overlay: After successful alignment of X-ray source and camera optical center, to enable an overlay of the images acquired by the X-ray device and video camera, a homography $H \in \mathbb{R}^{3\times 3}$ is estimated. This homography H is computed by a minimum of four corresponding points simultaneously detected in video and X-ray images such that $p_{(v,i)} = Hp_{(x,i)}$ with $p_{(v,i)}$ the 2-D point in the video image and $p_{(x,i)}$ the corresponding point in the X-ray image [41]. The computed homography compensates for differences both in intrinsic parameters and in orientation of the principle axis of projections (assuming that the position of the centers is previously aligned). Without loss of generality, any two projection matrices sharing the same projection center could be represented by $P_1 = K_1[I\ 0]$ and $P_2 = K_2[R\ 0]$ with $P_1, P_2 \in \mathbb{R}^{3\times 4}$ the projection matrices, $K_1, K_2 \in \mathbb{R}^{3\times 3}$

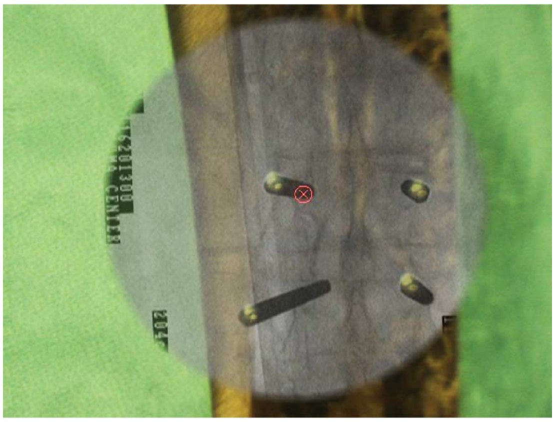

Fig. 7. Visualization of the image overlay system for dorsal spinal interventions. Four pedicle screws were placed with the system. The red crosshair defines one entry point for the awl or drill.

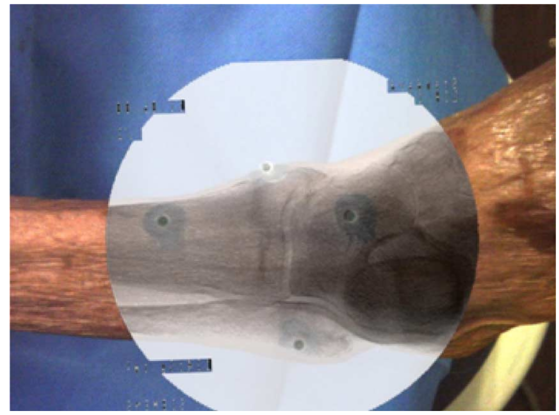

Fig. 8. Visualization of the image overlay for extremity, here a cadaver foot.

the camera matrices and $R \in \mathbb{R}^{3\times3}$ the relative orientation between the two cameras (direction of the principal axis). We have $P_2 = K_2 * R * K_1^{-1} P_1$, and the homography we are estimating is $H = K_2 * R * K_1^{-1}$, taking care of both changes in intrinsic parameters and extrinsic parameters. This is of course the case only for extrinsic parameters of two imaging devices which share the same projection center.

In practice, we implemented the estimation of a homography $H_{I_x \to I_v} \in \mathbb{R}^{3\times3}$, with I_v being the image of the video camera and I_x being the X-ray image in order to superimpose the X-ray image onto the video image. Any point p_x of the X-ray image can thus be wrapped to $p_{x\to v}$ its corresponding point on the video image I_v by $p_{x\to v} = H_{I_x \to I_v} p_x$. Within our application, we select four corresponding points $p_{v,i}$ in the video image and $p_{x,i}$ in the X-ray image interactively with the support of a subpixel accurate blob extraction algorithm. A semi-automatic establishment of the corresponding points is fine since the calibration has to be performed only once after the attachment of the video camera and the double mirror construction to the gantry and it is valid for a long time. The homography is computed by solving the linear equations system with the QR-Decomposition based on eight equations resulting from four corresponding points. In the most recent version, we use up to 16 points for the estimation of homography using DLT. The resulting matrix $H_{I_x \to I_v}$ can be visually validated using the resulting image overlay (cf. Fig. 8). As long as the video camera and the mirror construction is not moved with respect to the X-ray source, the calibration remains valid. The camera and mirror will be designed to remain inside the housing of the mobile C-arm and thus not be exposed to external forces, which could modify the rigid arrangement. This means that the physical alignment and the estimation of the homography have to be performed only once during construction of the device. An evaluation of the calibration accuracy was performed and is discussed in Section IV.

C. User Interface for Visualization and Navigation

The navigation software and user interface was developed in C++ based on our medical augmented reality framework (CAMPAR) [47] that is capable of temporal calibration and synchronization of various input signals (e.g., image and tracking data). The basic user interface allows an overlay of the X-ray onto the video image (cf. Figs. 7 and 8). Using standard mouse or touchscreen interaction a blending between fully opaque and fully transparent X-ray and the video image is possible. Once the down-the-beam position is identified, i.e., the direction of insertion is exactly in the direction of the radiation beam, an entry point can be identified in the X-ray image, which is directly visualized into the video image. The real time image overlay allows the surgeon to easily cut the skin for the instrumentation at the right location. It then provides the surgeon with direct feedback during the placement of the surgical instrument (e.g., guiding wire, awl, or drilling device) into the deep-seated target anatomy defined within the overlayed X-ray image (cf. Figs. 7 and 8). This comes without additional radiation for the patient and physician.

The image overlay is visualized on a standard monitor. This basic user interface was extended by a touchscreen monitor allowing easy interaction during the procedure. The touchscreen monitor can be covered and used in a sterile environment. A modular implementation allows a fast integration of workflow adopted visualization concepts [48] and control modules in order to extend system capabilities and customize the user interface. The current system setup requires only a limited user interaction for the calibration, the definition of entry point, and the control of blending factor of the X-ray overlay.

III. Clinical Applications

There is a wide range of potential clinical applications for the camera augmented mobile C-arm system. For procedures that are currently based on the intraoperative usage of mobile C-arms the new system can be integrated into the clinical procedure, since no additional hardware has to be set up and no time consuming on-site calibration or registration has to be performed before and during the procedure.

One requirement for the smooth integration of the camera augmented mobile C-arm system for needle placement and drilling applications is to position the C-arm in the so called *down-the-beam* position, i.e., that the direction of insertion is exactly in the direction of the radiation beam. After positioning the C-arm, the entry point has to be defined in the X-ray image. The entry point has to match the axis of the instrument during the insertion and is thus based on the exact *down-the-beam*

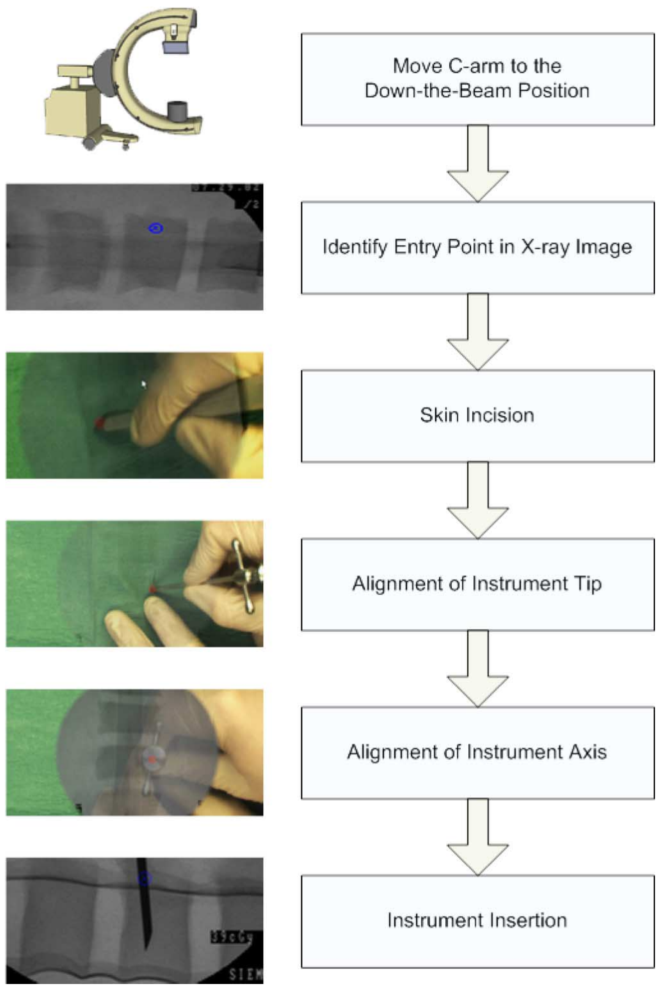

Fig. 9. Typical medical procedure for an instrument insertion using the camera augmented mobile C-arm system.

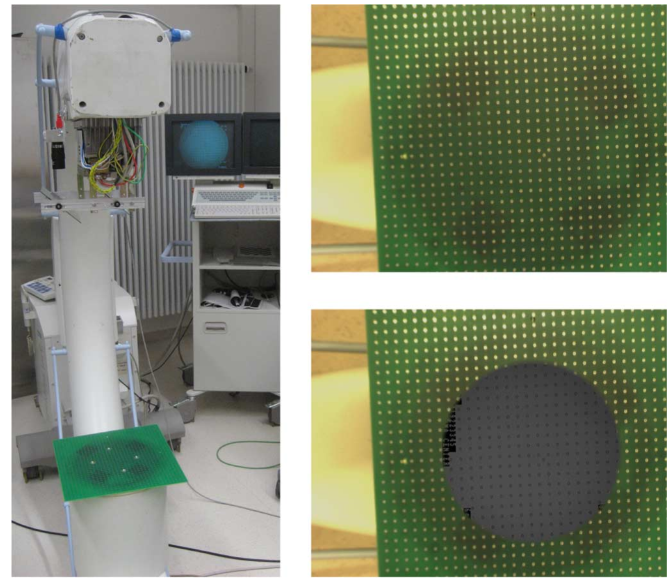

Fig. 10. X-ray calibration phantom is attached to the image intensifier in order to measure the image overlay accuracy. The right top shows the original image of the attached video camera and the right bottom shows the X-ray overlay onto the video camera image.

position of the C-arm and precise alignment of the instrument. The entry point is visualized also in the video image since the X-ray is coregistered with the video image by construction. Thus, the skin incision, the instrument tip alignment and the instrument axis alignment, i.e., to bring the instrument exactly in the *down-the-beam* position, can be done under video or fused video/X-ray control (cf. Fig. 9). Ideally, the entire insertion process is performed using only one single X-ray image. To control the insertion depth additional lateral X-ray images are routinely acquired.

To ensure a valid overlay of X-ray and video image, we attached markers that are simultaneously visible in both modalities. These markers can detect any miscalibration, if acquired X-ray image does not correctly overlay the video image. Furthermore, the markers are able to detect any patient or C-arm motion during usage of the system. The detection is sensitive to motions above 1 mm (cf. evaluation in Section IV-A2).

A. *Interlocking of Intramedullary Nails*

The procedure for distal interlocking of intramedullary nails can be difficult and time consuming. Several guiding techniques and devices have been proposed to aid the guiding of the distal holes [49]. Many techniques, especially the free hand techniques without the use of targeting apparatus expose the patient, surgeon and operation team to high doses of ionizing radiation. The camera augmented mobile C-arm can support the targeting of the distal holes and the locking procedure resulting in a considerable reduction of radiation dose. The C-arm is moved to the usual down-the-beam position. The fused image of X-ray and video then provides guidance for placement of the interlocking nail drilling, as well as screw insertion (cf. Fig. 12). The depth can be controlled by direct haptic feedback. The surgeon can feel the difference between drilling in bone and soft tissue. A lateral X-ray image is not required during this procedure since the depth control is of no clinical importance in this application.

B. *Percutaneous Spinal Interventions (Pedicle Approach)*

The pedicle approach for minimally invasive spinal interventions remains a challenging task even after a decade of image guided surgery. This has led to the development of a variety of computer aided techniques for dorsal pedicle interventions in the lumbar and thoracic spine [50], [7], [17]. Basic techniques use anatomical descriptions of the entry point and typical directions of the pedicle screws in conjunction with static X-ray control after instrumentation under intraoperative 2-D fluoroscopic control. Advanced techniques use CT-Fluoro, CT, 2-D or 3-D C-arm based navigation solutions.

The camera augmented mobile C-arm system can support the placement of the pedicle screws by means of an advanced visualization interface merging the real time video image and co-registered X-ray image. The only constraint for a proper use of the advanced visualization system is the down the beam positioning of the C-arm with respect to the pedicle of interest. The guidance procedure consists thus in the alignment of the instrument (e.g., k-wire) at the entry point (two degrees of freedom within the image plane) and then aligning the instrument within

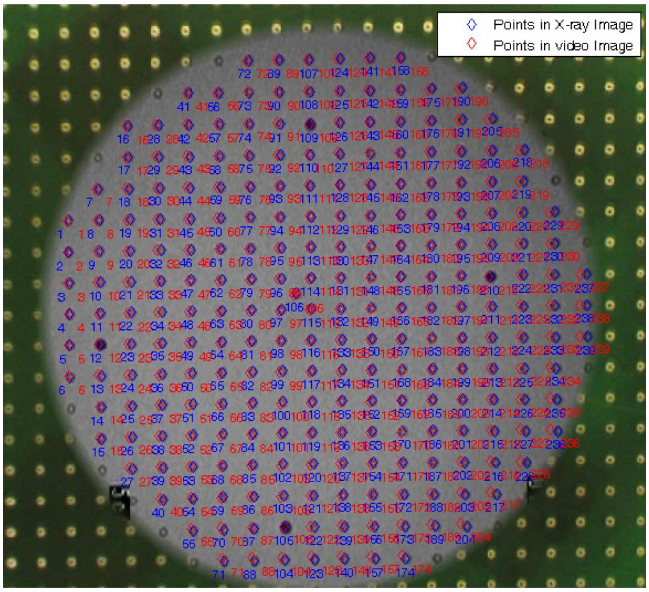

Fig. 11. Extracted centroids of markers of the calibration pattern in the video image (red) and in the X-ray image (blue) are overlaid onto the fused X-ray/video image.

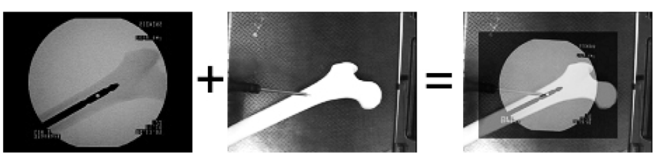

Fig. 12. Fused video and X-ray image during an intramedullary nail locking of the camera augmented mobile C-arm system provides a guidance interface ideally using only one X-ray image.

the viewing direction (two degrees of freedom for the axis orientation). Commonly used surgical instruments need minor modifications in order to make the axis of the instrument better visible within the camera view.

IV. Evaluation

For the evaluation of the designed and implemented camera augmented mobile C-arm system for instrument placement, we performed a series of experiments. The first set of experiments evaluates the technical accuracy of the system in terms of overlay and measures the radiation dose. The second set of experiments evaluates the feasibility of the navigation aid for clinical applications in terms of accuracy for the instrument guidance, X-ray radiation dose and success in task completion through phantom and cadaver studies.

A. Technical System Evaluation

1) System Accuracy Evaluation: In order to evaluate the calibration accuracy and thus the accuracy of the image overlay for the instrument guidance, we designed the following experiment to measure the influence of the orbital and angular rotation on the overlay accuracy. A pattern that is in general used for geometrical X-ray calibration and distortion measurement is attached to the image intensifier (cf. Fig. 10). The markers on the pattern are visible in both X-ray and video images (cf. Fig. 10) at the same time. The centroids of the markers are extracted in both images with subpixel accuracy and used to compute the distance between corresponding point pairs. The markers in the video and X-ray image are detected using a template matching algorithm. The centroids are computed using an intensity weighted algorithm. The distances between the centroids in the video image and transformed X-ray image is computed in subpixel accuracy for all detected points in both images.

TABLE I
Difference in Pixel (PX) Between the Extracted Marker Centroids in the Video Image and Transformed, Overlaid X-Ray Image for Three Different Calibration Runs

trial number	#1	#2	#3
mean (px)	1.39	1.98	1.38
std (px)	0.85	0.99	0.76
max (px)	4.76	5.02	3.89
number of control points	234	237	208

TABLE II
Difference in Pixel (PX) Between the Extracted Marker Centroids in the Video Image and Transformed, Overlaid X-Ray Image for Different Orbital Rotations

	0°	15°	30°	60°	90°
	orbital rotation				
mean (px)	1.59	2.81	5.13	9.48	12.33
std (px)	0.87	1.05	1.10	2.57	4.15
max (px)	5.02	7.13	9.55	14.67	19.45
# points	679	239	236	232	229
	orbital rotation with re-estimated homography				
	0°	15°	30°	60°	90°
mean (px)	1.59	2.29	2.66	2.87	2.76
std (px)	0.87	1.07	1.25	1.17	1.16
max (px)	5.02	5.76	6.61	6.67	6.53
# points	679	238	235	237	238

The camera positioning and calibration step was performed three times. The mean error of the control points was 1.59 ± 0.87 pixels with a maximum error of 5.02 pixels. On the image plane of the calibration pattern three pixels correspond to 1 mm, thus the mean error is approximately 0.5 mm on the plane of the calibration pattern. See Table I for details on the calibration accuracy.

The same experiment with the attached calibration phantom was also conducted with different angular and orbital rotations. In all angular and orbital poses, we analyzed the overlay accuracy with and without a per-pose estimation of the homography based on four optical and X-ray visible markers. Table II presents the measurement errors for orbital rotations and Table III for angular rotations, respectively. The mean overlay error was found to be constant during orbital and angular rotation of the C-arm, if a re-estimation of the homography is performed at the specific C-arm position. In the cases where the homography was not re-estimated, i.e., the homography was estimated in the original position of the C-arm with no orbital and angular rotation and applied for other poses of the C-arm, the mean error of the points increase with an increase in the rotation angle. The experiments confirm that a per-pose re-estimation of the homography results in an accurate image overlay. Building a clinical solution, one could easily ensure the correct per-pose re-estimation of the required parameters

TABLE III
DIFFERENCE IN PIXEL (PX) BETWEEN THE EXTRACTED MARKER CENTROIDS IN THE VIDEO IMAGE AND TRANSFORMED, OVERLAID X-RAY IMAGE FOR DIFFERENT ANGULAR ROTATIONS

	0°	15°	30°	60°	90°
	angular rotation				
mean (px)	1.59	2.86	4.81	7.89	9.61
std (px)	0.87	0.99	0.92	1.98	3.07
max (px)	5.02	5.83	7.35	12.54	15.21
# points	679	237	236	230	231
	angular rotation with re-estimated homography				
	0°	15°	30°	60°	90°
mean (px)	1.59	1.35	1.42	1.33	1.56
std (px)	0.87	0.84	0.96	0.94	1.00
max (px)	5.02	4.41	4.95	4.67	5.08
# points	679	233	236	236	237

TABLE IV
DETECTION ACCURACY OF MARKERS. THE MARKERS WERE MECHANICALLY MOVED AND THE OVERLAY ACCURACY WAS ESTIMATED IN PIXEL

marker movement (mm)	0	0.5	1	1.5	2
mean (px)	0.9	0.9	1.46	2.26	3.09

TABLE V
VERTEBROPLASTY EXPERIMENT ON FIVE FOAM EMBEDDED SPINE PHANTOMS. TIME IS MEASURED IN MINUTES: SECONDS. RADIATION IN RADIATION MINUTES

	#1	#2	#3	#4	#5
overall duration	15:00	20:10	17:00	9:15	14:46
overall radiation	0.4	0.2	0.4	0.1	0.5
setup time	2:31	0.38	0:20	0:45	2:33
insertion time	8:05	14:32	13:00	5:30	5:11
filling time	4:24	5:00	3:40	3:00	7:02
setup radiation	0.3	0.0	0.0	0.0	0.1
insertion radiation	0.1	0.2	0.4	0.1	0.2
filling radiation	0.1	0.0	0.0	0.0	0.2
placement cat.	A	A	A	B	C

for the planar transformation between the images. Therefore, the results of Table III could be considered as reference.

2) Evaluation of Marker Tracking Accuracy: In addition to the overlay accuracy, we have also assessed the accuracy of marker detection. An experiment was designed in which we moved the marker on a submillimeter accurate mechanical device and computed the deviation of the overlaid marker. For this experiment, the mechanical device was rigidly attached to the detector plane and moved in 0.5 mm steps. Table IV shows the results of this experiment. The results suggest that a motion of 1 mm and more can be detected. The threshold to notify the surgeon about a non valid overlay was set to 1.5 pixel according to this and the previous experiment on overlay accuracy.

3) Radiation Dose Evaluation: Radiation dose considerations with various C-arm positions and orientations are well studied in literature [51]. The under the table positioning of X-ray source is generally recommended in order to reduce scattered radiation to the surgeon's head and neck. It is however important to notice that all C-arm systems have been carefully evaluated by relevant authorities and certified for their use in all configurations. In routine surgeries over the table and lateral positions of the C-arm are also used according to the anatomic target of interest, clinical application and surgical preferences. When using the CAMC for the clinical applications discussed in this paper, the X-ray is positioned over the table, however thanks to the use of the coregistered optical images the overall number of X-ray acquisitions are dramatically reduced and therefore the overall radiation dose to both patient and clinical staff is expected to be considerably reduced. It is also important to make sure that the addition of the mirror construction does not affect the X-ray image quality. Within our setup, the C-arm system was modified by a mirror construction between the X-ray source and image intensifier (detector). Initially, there was no loss of X-ray image quality recognized by the surgeons after the attachment of the mirror construction. However, to quantify this absorbtion of radiation, we assessed the radiation dose with and without the attached mirror construction. We used the external radiation dose measurement device Unfors Xi from Unfors Instruments GmbH (Ulm, Germany). The measured radiation dose on the detector plane with the mirror was in average 38% lower than its corresponding value without the mirror construction on the path of the X-ray beam. This was assessed with tube voltage 64 kv, 70 kv, and 77 kv. Within our final setup, the C-arm X-ray beam was internally adjusted such that the applied radiation dose at the detector plan did not change after attaching the mirrors. Thus the absorption of the mirror construction was compensated for. The mirror homogeneously covers the radiation beam. Thus, there is no impact on the image quality of the final X-ray image.

The objective of a further test for assessing the radiation dose was to measure the applied radiation dose of the camera augmented mobile C-arm with the X-ray source above the patient. Within different setups of the radiation measurement device attached to the image intensifier with and without the patient bed, as well as the radiation measurement device attached to the bed, all measurements with the same tube voltage 64 kV, we measured different radiation doses. As the distance to the X-ray source increases the radiation dose reduces considerably. Furthermore, the table absorbs around 30% of the radiation dose. Within real patient setups, this has to be assessed considering that with the camera augmented mobile C-arm system the table is not absorbing any radiation before it is delivered to the patient, but the distance to the X-ray source is slightly increased. In the first configuration, the patient bed is removed and we measure the radiation received directly on the image intensifier to be 22 μGy. In the second configuration, the measurement device remains at its position on the image intensifier while the bed is positioned between the X-ray source and image intensifier. The dose was measured to be 15 μGy. In the third configuration, where the bed remains in the last position while the measurement device is moved on the top of the bed, the measured dose was 31 μGy. This approximately measures the radiation dose to be received by the patient. In addition, several radiation measurements were done using the external dose-area product measurement device to ensure the safety of the surgical team. Note that the housing is covered with lead foil to reduce the scattered radiation of the mirror construction on the head and eye level of the operating team. Within all measurements that were made outside the direct radiation beam for both configurations, in which the source is above and under the bed, no measurable radiation could be detected. Scattered radiation of the patient was ignored throughout all experiments and has to be validated

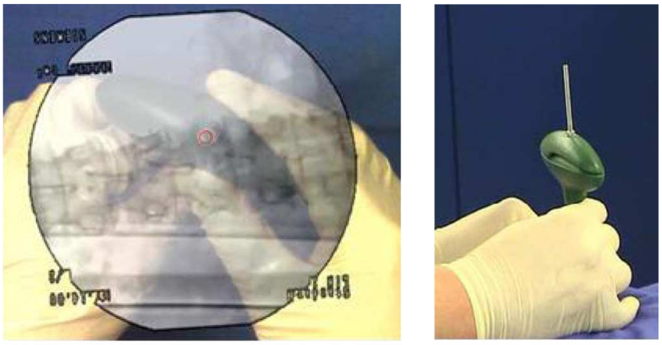

(a) (b)

Fig. 13. Cadaver study for pedicle approach with a modified needle tool that is extended by a k-wire to align the instrument axis in the *down-the-beam* position. (a) *Down-the-beam* alignment and (b) modified needle tool.

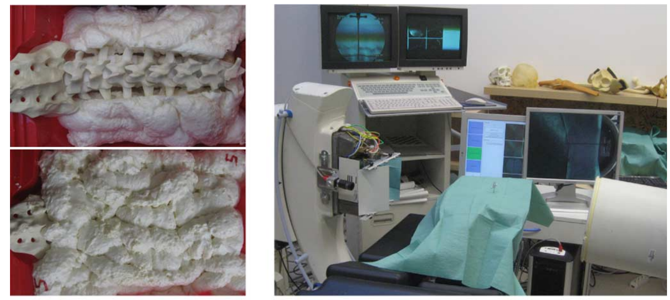

(a) (b)

Fig. 14. Phantom experiment for the vertebroplasty procedure. (a) Embedded spine phantom and (b) system setup for the simulated procedure.

through initial clinical trials. The local protection radiation authorities approved the upside–down configuration for its usage in the OR within the described experiments.

B. Preclinical Evaluation

1) Cadaver Studies for Interlocking of Intramedullary Nails: We performed a cadaver study for the interlocking of intramedullary nails. Commonly used surgical instruments needed modifications in order to better identify the axis of the instruments under video-control in the *down-the-beam* position. Updated fluoroscopic images could be obtained at any time during the intervention. The surgical procedure was not compromised compared to fluoroscopic guided intramedullary nail locking and the user-interface provided intuitive control of the nail insertion. The procedure performed with the camera augmented mobile C-arm showed advantages over standard C-arm based interlocking techniques (cf. Fig. 12). A maximum of two X-ray images were required for placing a interlocking screw. The camera augmented mobile C-arm system provided a rich opto-X-ray view for positioning and orientation of the drilling device. Drill-hole identification was possible in all cases.

2) Cadaver Studies for Pedicle Screw Placement: Together with our surgical partner, we performed two cadaver studies in different levels of the lumbar and thoracic spine using a percutaneous pedicle approach. We evaluated the placement of the screws by a postinterventional CT and the dissection of the placed pedicle. The entry point was defined in the X-ray image and the placement of the tool-tip and its alignment was carried out under video-control. After the alignment of the tool axis in the *down-the beam* position, the insertion was performed [cf. Fig. 13(a)]. If additional X-ray and video opaque markers did not coincide in video and X-ray images, the patient had moved and therefore we acquired an additional X-ray image that was by construction coregistered with the video image. Modified instruments were required in order to better identify the instrument axis [cf. Fig. 13(b)]. The experiments showed that the camera augmented mobile C-arm system provides a reliable and robust two dimensional visualization for guided pedicle screw insertion. The one time calibration was stable during the whole series of both experiments even if it is not yet perfectly shielded against exposure to external forces in our laboratory setup. During spinal interventions through the pedicle, a maximum of three X-ray images were required for the instrument insertion. This presents a reduction compared to standard C-arm based procedures. The study showed that we were close to the theoretical value of only one single X-ray image for the pedicle screw placement procedure. However, new X-ray images were acquired during the procedure for updating the intervention in terms of patient movement and implant placement control by direct imaging. The radiation time and dose was considered to be less compared to the same procedure only guided by a C-arm system. Pedicle identification and needle insertion was possible in all cases.

3) Simulated Procedure for Vertebroplasty: For a structured preclinical evaluation, we designed a series of experiments to analyze the duration and radiation time of the proposed procedure as well as the placement accuracy of the instrumentation. Therefore, we embedded five spine phantoms (T10–T12 and L1–L5) within a foam cover [cf. Fig. 14(a)]. Using these phantoms we simulated the complete process for vertebroplasty [52] on the first lumbar vertebra (L1) as target anatomy. The anatomy of the L1 in the phantom was identical in all cases. There was also no variation in the anatomy of the vertebra. We defined the entry point and inserted the cannula for cement filling using the camera augmented mobile C-arm system. We measured the overall duration, the overall radiation dose, as well as the required duration and dose for the system setup, the guided instrument insertion and the cement filling of the vertebra.

The procedure requires the insertion of a guiding wire and filling cannula through the pedicle of the vertebra, similar to the access route described for pedicle screw placement in the cadaver studies in the previous Section IV-B2

Within our experiments three out of five needles were perfectly positioned, i.e., in central position through the pedicle of the L1 (classification group A according to Arand *et al.* [53]). Within the other two experiments the access path showed medial perforation (classification group B and C) according to Arand *et al.* [53]). The observation of the videos recorded by our workflow analysis tool of these two experiments showed an undetected motion of the phantom. The automatic detection of displacement by markers that are simultaneously visible in the video camera and X-ray image generates a feedback to the surgeon in order to correct the situation by simply taking a new

X-ray image. This has been already implemented and used to detect relative patient/C-arm movement greater than 1 mm, which will result in a detectable misalignment of the overlaid images, see experimental results presented in Section IV-A2.

V. Discussion and Conclusion

We presented an advanced imaging system that extends a mobile C-arm by an optical video camera and a double mirror construction. We propose and evaluate various applications for orthopedics and trauma surgery that benefit from the new system. Within orthopedics and trauma surgery procedures, image guidance by mobile C-arm is a standard task in everyday clinical routine. CAMC allows the surgeon to have at least the same performance he/she has under traditional fluoroscopic control without introduction of additional devices, e.g., external tracking systems, or extra operative tasks. After the camera attachment and joint X-ray optical calibration procedure, all taken X-ray images are by default coregistered with the video image and the system provides thus an advanced visualization for *down-the-beam* instrumentation, ideally with the acquisition of only one single X-ray image.

We performed a technical system analysis in terms of image overlay accuracy. From the conducted experiments we can conclude, that a per-pose estimation of the X-ray and optical images is required to achieve sufficient image overlay accuracy. We use the Direct Linear Transform (DLT) method to estimate the homography using once 4 and then 12 point correspondences. We then tested the overlay accuracy using the remaining four markers, which were not used for homography estimation. We repeated the same experience selecting different subsets of points. The use of 12 markers instead of 4 only decreased the average error of the image overlay from 1.05 mm to 0.92 mm with comparable standard deviations of 0.52 mm and 0.49 mm. This is most probably due to the high precision with which, we can detect the markers in our calibration setup. The new generation of C-arms have encoded the projection matrices for every orientation of the C-arm e.g., for reconstruction purposes. For the clinical applicability, the homography can be encoded in addition to the projection matrices. Sterilizable X-ray/video visible marker patterns attached to the patients surface within the X-ray scan area can be used for an additional conformity test and/or recalibration of the homography.

The clinical feasibility and accuracy of implant placement was evaluated through different cadaver studies and simulated procedures on phantoms for different clinical applications. We added a real-time detection of combined Opto-X-ray markers in the surgical scene to detect patient or C-arm motion. Thus the system will inform the surgeon about any misalignment, which will result in the acquisition of just one additional X-ray image. Intramedullary nail locking is a very promising application since there is only a requirement for the lateral positioning of the instrument to target the interlocking hole, but no requirement for image guidance of the insertion depth. The physician defines the insertion depth thanks to haptic feedback using the difference in the force feedback between bone and soft tissue during the drilling and screwing process. Another evaluated application was the pedicle approach in the spine. This included pedicle screw placement and vertebroplasty procedures. Both applications show promising results. Previously presented application domains for the camera augmented mobile C-arm, which are not discussed here are needle placement [54], [37], X-ray geometric calibration [40], and positioning and repositioning of C-arm based on visual servoing [55].

As the camera augmented mobile C-arm system is integrated into the mobile C-arm, no extra hardware like external tracking cameras or additional monitors are needed. Surgery can start instantly without any delay caused by calibration of tools or patient registration. The hardware-modifications in this guidance prototype lead to a slightly reduced distance between the housing of the radiation source and image intensifier (around 6 cm) and the C-arm has to be used in upside–down configuration. The slightly shorter working volume could be a limitation for applications in the shoulder and hip region, since in these applications large rotational orbit is desired which in turn requires a larger free space within the gantry. A lead shielding of the housing of the camera and mirror setup guarantees that there is no measurable additional radiation for the surgeon and surgical staff. With the new generation of C-arms based on flat panel technology instead of image intensifier, the current limitations of reduced distance between source and detector and the need for geometric distortion are both alleviated.

The integrated camera augmented mobile C-arm system has high potential to be introduced in everyday surgical routine, reduce the currently applied high radiation dose, and augment the surgeon's vision of the operation situs.

Acknowledgment

The authors would like to thank R. Graumann, Siemens Medical Solutions SP, for his continuous support. The authors would also like to thank the two additional co-inventors of the camera augmented mobile C-arm system: M. Mitschke and A. Bani-Hashemi. The authors would also like to thank L. Wang, S. Benhimane, S. Wiesner, H. Heibel, D. Zaeuner, P. Dressel, and A. Ahmadi for their technical support within the NARVIS Laboratory. Finally, the authors would like to thank Dr. E. Euler and Dr. W. Mutschler for their medical advice during the design and evaluation of the system.

References

[1] B. M. Boszczyk, M. Bierschneider, S. Panzer, W. Panzer, R. Harstall, K. Schmid, and H. Jaksche, "Fluoroscopic radiation exposure of the kyphoplasty patient," *Eur. Spine J.*, vol. 15, no. 3, pp. 347–355, Mar. 2006.

[2] M. Synowitz and J. Kiwit, "Surgeon's radiation exposure during percutaneous vertebroplasty," *J. Neurosurg. Spine*, vol. 4, no. 2, pp. 106–109, Feb. 2006.

[3] Y. R. Rampersaud, K. T. Foley, A. C. Shen, S. Williams, and M. Solomito, "Radiation exposure to the spine surgeon during fluoroscopically assisted pedicle screw insertion," *Spine*, vol. 25, no. 20, pp. 2637–2645, Oct. 2000.

[4] N. Theocharopoulos, K. Perisinakis, J. Damilakis, G. Papadokostakis, A. Hadjipavlou, and N. Gourtsoyiannis, "Occupational exposure from common fluoroscopic projections used in orthopaedic surgery," *J. Bone Joint Surg. Amer.*, vol. 85, pp. 1698–1703, Oct. 2003.

[5] B. Jaramaz and I. A. M. DiGioia, "CT-based navigation systems," in *Navigation and Robotics in Total Joint and Spine Surgery*, J. B. Stiehl, W. H. Konermann, and R. G. A. Haaker, Eds. New York: Springer, 2003, ch. 2, pp. 10–16.
[6] A. M. DiGioia, B. Jaramaz, F. Picard, and L.-P. Nolte, Eds., *Computer and Robotic Assisted Hip and Knee Surgery*. New York: Oxford Univ. Press, 2004.
[7] J. M. Mathis, Ed., *Image-Guided Spine Interventions*. New York: Springer, 2004.
[8] J. Stiehl, W. Konermann, and R. Haaker, Eds., *Navigation and Robotics in Total Joint and Spine Surgery*. New York: Springer, 2004.
[9] J. B. Stiehl, W. H. Konermann, R. G. Haaker, and A. DiGioia, Eds. *Navigation and MIS in Orthopedic Surgery*. New York: Springer, 2006.
[10] T. Laine, T. Lund, M. Ylikoski, J. Lohikoski, and D. Schlenzka, "Accuracy of pedicle screw insertion with and without computer assistance: A randomised controlled clinical study in 100 consecutive patients," *Eur. Spine J.*, vol. 9, no. 3, pp. 235–240, 2000.
[11] Y. Kotani, K. Abumi, M. Ito, M. Takahata, H. Sudo, S. Ohshima, and A. Minami, "Accuracy analysis of pedicle screw placement in posterior scoliosis surgery: Comparison between conventional fluoroscopic and computer-assisted technique," *Spine*, vol. 32, no. 14, pp. 1543–1550, Jun. 2007.
[12] S. Rajasekaran, S. Vidyadhara, P. Ramesh, and A. P. Shetty, "Randomized clinical study to compare the accuracy of navigated and non-navigated thoracic pedicle screws in deformity correction surgeries," *Spine*, vol. 32, no. 2, pp. E56–E64, Jan. 2007.
[13] F. Langlotz and L. Nolte, "Computer-assisted minimally invasive spine surgery—State of the art," in *Minimally Invasive Spine Surgery—A Surgical Manual*, H. M. Mayer, Ed. New York: Springer, 2006, ch. 6, pp. 26–32.
[14] K. Foley, D. Simon, and Y. Rampersaud, "Virtual fluoroscopy: Computer-assisted fluoroscopic navigation," *Spine*, vol. 26, no. 4, pp. 347–351, 2001.
[15] J. H. Siewerdsen, D. J. Moseley, S. Burch, S. K. Bisland, A. Bogaards, B. C. Wilson, and D. A. Jaffray, "Volume CT with a flat-panel detector on a mobile, isocentric c-arm: Pre-clinical investigation in guidance of minimally invasive surgery," *Med. Phys.*, vol. 32, no. 1, pp. 241–254, Jan. 2005.
[16] D. Ritter, M. Milschke, and R. Graumann, "Markerless navigation with the intra-operative imaging modality siremobil iso-c^{3D}," *Electromedica*, vol. 70, no. 1, pp. 31–36, 2002.
[17] E. Euler, S. Heining, C. Riquarts, and W. Mutschler, "C-arm-based three-dimensional navigation: A preliminary feasibility study," *Comput. Aided Surg.*, vol. 8, no. 1, pp. 35–41, 2003.
[18] M. Hayashibe, N. Suzuki, A. Hatlori, Y. Otake, S. Suzuki, and N. Nakata, "Surgical navigation display system using volume rendering of intraoperatively scanned CT images," *Comput. Aided Surg.*, vol. 11, no. 5, pp. 240–246, Sep. 2006.
[19] C. Mehlman and T. DiPasquale, "Radiation exposure to the surgical team during fluoroscopy: "How far is far enough?"," *Orthop. Trauma*, vol. 11, pp. 392–398, 1997.
[20] F. Gebhard, M. Kraus, E. Schneider, M. Arand, L. Kinzl, A. Hebecker, and L. Bätz, "Radiation dosage in orthopedics—A comparison of computer-assisted procedures," *Unfallchirurg*, vol. 106, no. 6, pp. 492–497, 2003.
[21] A. P. King, P. J. Edwards, C. R. Maurer Jr., D. A. De Cunha, D. J. Hawkes, D. L. G. Hill, R. P. Gaston, M. R. Fenlon, A. J. Strong, C. L. Chandler, A. Richards, and M. J. Gleeson, "Design and evaluation of a system for microscope-assisted guided interventions," *IEEE Trans. Med. Imag.*, vol. 19, no. 11, pp. 1082–1093, Nov. 2000.
[22] P. Paul, O. Fleig, and P. Jannin, "Augmented virtuality based on stereoscopic reconstruction in multimodal image-guided neurosurgery: Methods and performance evaluation," *IEEE Trans. Med. Imag.*, vol. 24, no. 11, pp. 1500–1511, Nov. 2005.
[23] W. Birkfellner, M. Figl, K. Huber, F. Watzinger, F. Wanschitz, J. Hummel, R. Hanel, W. Greimel, P. Homolka, R. Ewers, and H. Bergmann, "A head-mounted operating binocular for augmented reality visualization in medicine—Design and initial evaluation," *IEEE Trans. Med. Imag.*, vol. 21, no. 8, pp. 991–997, Aug. 2002.
[24] W. E. L. Grimson, T. Lozano-Perez, W. M. Wells, G. J. Ettinger, S. J. While, and R. Kikinis, "An automatic registration method for frameless stereotaxy, image guided surgery, and enhanced reality visualization," *IEEE Trans. Med. Imag.*, vol. 15, no. 2, pp. 129–140, Apr. 1996.
[25] M. Bajura, H. Fuchs, and R. Ohbuchi, "Merging virtual objects with the real world: Seeing ultrasound imagery within the patient," in *Proc. 19th Annu. Conf. Comput. Graphics Interactive Techniques*, 1992, pp. 203–210.
[26] A. State, D. T. Chen, C. Tector, A. Brandt, H. Chen, R. Ohbuchi, M. Bajura, and H. Fuchs, "Case study: Observing a volume rendered fetus within a pregnant patient," in *Proc. Conf. Visualizat.*, 1994, pp. 364–368.
[27] F. Sauer, A. Khamene, B. Bascle, and G. J. Rubino, "A head-mounted display system for augmented reality image guidance: Towards clinical evaluation for imri-guided neurosurgery," in *Proc. Int. Conf. Med. Image Computing Computer Assist. Intervent. (MICCAI)*, London, U.K., 2001, pp. 707–716.
[28] F. Sauer, U. J. Schoepf, A. Khamene, S. Vogt, M. Das, and S. G. Silverman, "Augmented reality system for ct-guided interventions: System description and initial phantom trials," in *Med. Imag.: Visualiz., Image-Guided Procedures, Display*, 2003, pp. 179–190.
[29] M. Blackwell, C. Nikou, A. M. DiGioia, and T. Kanade, "An image overlay system for medical data visualization," *Med. Imag. Anal.*, vol. 4, no. 1, pp. 67–72, 2000.
[30] T. Sielhorst, M. Feuerstein, and N. Navab, "Advanced medical displays: A literature review of augmented reality," *IEEE/OSA J. Display Technol.*, vol. 4, no. 4, pp. 451–467, Dec. 2008.
[31] G. D. Stetten, A. Cois, W. Chang, D. Shelton, R. J. Tamburo, J. Castellucci, and O. Von Ramm, "C-mode real lime lomographic reflection for a malrix array ultrasound sonic flashlight," in *Proc. Int. Conf. Med. Image Computing Computer Assisted Intervent. (MICCAI)*, R. E. Ellis and T. M. Peters, Eds., 2003.
[32] G. Fichtinger, A. Deguet, K. Masamune, E. Balogh, G. S. Fischer, H. Mathieu, R. H. Taylor, S. J. Zinreich, and L. M. Fayad, "Image overlay guidance for needle insertion in cl scanner," *IEEE Trans. Biomed. Eng.*, vol. 52, no. 8, pp. 1415–1424, Aug. 2005.
[33] G. S. Fischer, A. Deguet, D. Schlattman, L. Fayad, S. J. Zinreich, R. H. Taylor, and G. Fichtinger, "Image overlay guidance for MRI arthrography needle insertion," *J. Comput. Aided Surg.*, vol. 12, no. 1, pp. 2–14, 2007.
[34] J. Leven, D. Burschka, R. Kumar, G. Zhang, S. Blumenkranz, X. D. Dai, M. Awad, G. D. Hager, M. Marohn, M. Choti, C. Hasser, and R. H. Taylor, "Davinci canvas: A telerobotic surgical system with integrated, robot-assisted, laparoscopic ultrasound capability," in *Proc. Int. Conf. Med. Image Computing Computer Assisted Intervent. (MICCAI)*, Sep. 2005, vol. 3749, pp. 811–818.
[35] M. Feuerstein, T. Mussack, S. M. Heining, and N. Navab, "Intra-operative laparoscope augmentation for port placement and resection planning in minimally invasive liver resection," *IEEE Trans. Med. Imag.*, vol. 27, no. 3, pp. 355–369, Mar. 2008.
[36] T. Wendler, M. Feuerstein, J. Traub, T. Lasser, J. Vogel, F. Daghighian, S. Ziegler, and N. Navab, "Real-time fusion of ultrasound and gamma probe for navigated localization of liver metastases," in *Proc. Int. Conf. Medical Image Computing Computer Assist. Intervent. (MICCAI)*, N. Ayache, S. Ourselin, and A. Maeder, Eds., Brisbane, Australia, Oct./Nov. 2007, vol. 4792, pp. 252–260.
[37] M. Mitschke, A. Bani-Hashemi, and N. Navab, "Interventions under video-augmented x-ray guidance: Application to needle placement," in *Proc. Int. Conf. Med. Image Computing Computer Assist. Intervent. (MICCAI)*, Oct. 2000, vol. 1935, pp. 858–868.
[38] N. Navab, M. Mitschke, and A. Bani-Hashemi, "Merging visible and invisible: Two camera-augmented mobile C-arm (CAMC) applications," in *Proc. IEEE and ACM Int. Workshop on Augmented Reality*, San Francisco, CA, 1999, pp. 134–141.
[39] M. Mitschke and N. Navab, "Recovering projection geometry: How a cheap camera can outperform an expensive stereo system," in *Proc. IEEE Conf. Comput. Vis. Pattern Recognit. (CVPR)*, 2000, vol. 1, pp. 193–200.
[40] M. Mitschke and N. Navab, "Recovering X-ray projection geometry for 3d tomographic reconstruction: Use of integrated camera vs. external navigation system," *Int. J. Med. Image Anal.*, vol. 7, no. 1, pp. 65–78, Mar. 2003.
[41] R. Hartley and A. Zisserman, *Multiple View Geometry in Computer Vision*, 2nd ed. New York: Cambridge Univ. Press, 2003.
[42] J. G. Semple and G. T. Kneebone, *Algebraic Projective Geometry*. New York: Oxford Univ. Press, 1998.

[43] N. Navab and M. Mitschke, “Method and apparatus using a virtual detector for three-dimensional reconstruction form X-ray images,” U.S. 6236704, Jun. 30, 1999.

[44] R. Tsai, “A versatile camera calibration technique for high accuracy 3d machine vision metrology using off-the-shelf TV cameras and lenses,” *IEEE J. Robot. Automat.*, vol. RA-3, no. 4, pp. 323–344, 1987.

[45] J. Heikkilä and O. Silvén, “A four-step camera calibration procedure with implicit image correction,” in *Proc. IEEE Conf. Comput. Vis. Pattern Recognit. (CVPR)*, 1997, pp. 1106–1112.

[46] Z. Zhang, “A flexible new technique for camera calibration,” *IEEE Trans. Pattern Anal. Mach. Intell.*, vol. 22, no. 11, pp. 1330–1334, Nov. 2000.

[47] T. Sielhorst, M. Feuerstein, J. Traub, O. Kutter, and N. Navab, “Campar: A software framework guaranteeing quality for medical augmented reality,” *Int. J. Comput. Assist. Radiol. Surg.*, vol. 1, no. 1, pp. 29–30, Jun. 2006.

[48] N. Navab, J. Traub, T. Sielhorst, M. Feuerstein, and C. Bichlmeier, “Action- and workflow-driven augmented reality for computer-aided medical procedures,” *IEEE Comput. Graph. Applicat.*, vol. 27, no. 5, pp. 10–14, Sep./Oct. 2007.

[49] G. M. Whatling and L. D. Nokes, “Literature review of current techniques for the insertion of distal screws into intramedullary locking nails injury,” *Injury*, vol. 37, no. 2, pp. 109–119, Feb. 2005.

[50] R. A. Hart, B. L. Hansen, M. Shea, F. Hsu, and G. J. Anderson, “Pedicle screw placement in the thoracic spine: A comparison of image-guided and manual techniques in cadavers,” *Spine*, vol. 30, no. 12, pp. 326–331, Jun. 2005.

[51] M. Fuchs, H. Modler, A. Schmid, and K. M. Stürmer, “Strahlenschutz im operationssaal,” *Operative Orthopdie Traumatologie*, vol. 11, no. 4, pp. 328–333, 1999.

[52] J. M. Mathis, H. Deramond, and S. M. Belkoff, Eds., *Percutaneous Vertebroplasty and Kyphoplasty*, 2nd ed. New York: Springer, 2006.

[53] M. Arand, E. Hartwig, D. Hebold, L. Kinzl, and F. Gebhard, “Präzisionsanalyse navigationsgestützt implantierter thorakaler und lumbaler pedikelschrauben,” *Unfallchirurg*, vol. 104, no. 11, pp. 1076–1081, 2001.

[54] M. H. Loser and N. Navab, “A new robotic system for visually controlled percutaneous interventions under CT fluoroscopy,” in *Proc. Med. Image Computing Computer Assisted Interventions (MICCAI)*, Pittsburgh, PA, Oct. 2000, pp. 887–896.

[55] N. Navab, S. Wiesner, S. Benhimane, E. Euler, and S. M. Heining, “Visual servoing for intraoperative positioning and repositioning of mobile c-arms,” in *Proc. Int. Conf. Medical Image Computing Computer Assisted Intervention (MICCAI)*, Copenhagen, Denmark, Oct. 2006, pp. 551–560.